DESIGN AND SIMULATION OF AN UNDERACTUATED END-EFFECTOR FOR LOW-DAMAGE SWEET PEPPER HARVESTING

, *欠驱动式甜椒低损采摘机械手的设计与仿真验证*

Caiqi HU^{1,2)}, Dongyu LIU^{1,2)}, Jing JI^{*1)}, Siyuan ZHENG^{1,2)}, Yichen LI^{1,2)}, Junhao LI^{1,2)}

Keywords: Sweet pepper; Non-destructive harvesting; End-effector; Underactuation; ADAMS

ABSTRACT

This paper presents the design of a linkage-based underactuated end-effector for sweet pepper harvesting. The end-effector employs a single motor to drive a spring differential system, enabling two three-phalanx fingers to sequentially and adaptively envelop the fruit in a proximal-middle-distal order, coupled with a pneumatic cutting mechanism for peduncle separation. Biomechanical tests on sweet peppers established a safe grasping force threshold range of 0.72 N to 33.56 N. The phalanx dimensions were optimized using a genetic algorithm, ensuring the workspace covers the fruit diameter range of 70–103 mm. Static analysis determined that the push rod inclination angle should be maintained between 5°–10° to avoid dead points. ADAMS simulations verified the effectiveness of the enveloping sequence, with a peak contact force of 15.89 N remaining within non-destructive range. Prototype tests demonstrated that at a rotational speed of 90 r/min, the harvesting success rate reached 89.34%, the single-fruit harvesting time was 21.70 s, and the damage rate was 0%, confirming the effectiveness and feasibility of the proposed mechanism for low-damage sweet pepper harvesting.

摘要

本文设计了一种基于欠驱动原理的连杆式甜椒采摘末端执行器,通过单电机驱动弹簧差动系统,实现两指三指节按序自适应包络果实,并配合气动剪切机构分离果柄。通过甜椒生物力学试验获得夹持力安全阈值为 0.72N 至 33.56N,利用遗传算法优化指节尺寸,使工作空间覆盖 70–103 mm 果径范围。静力学分析确定推杆倾角宜控制在 5°-10°以避免死点。ADAMS 仿真验证了包络时序合理,接触力峰值 15.89 N 处于无损范围内。样机试验表明,在 90 r/min 转速下,采摘成功率达 89.34%,单果耗时 21.70 s,损伤率为 0,验证了机构在甜椒低损采摘方面的有效性与可行性。

INTRODUCTION

Sweet pepper, as a high-value economic crop, holds a significant position in the international agricultural market due to its unique flavor and nutritional value. China, as a major global producer of sweet peppers, accounts for approximately 35% of the world's cultivation area (*Chen et al., 2025; Wang et al., 2023*). According to statistics from the Ministry of Agriculture and Rural Affairs, as of 2023, the domestic sweet pepper cultivation area reached 250,000 hectares, with an annual output of about 3.5 million tons, primarily relying on open-field and greenhouse production modes. However, field investigations indicates that sweet pepper harvesting is still predominantly manual, characterized by low efficiency, with labor costs accounting for up to 45% of the total production cost. With the increasing shortage of rural labor, developing efficient, low-damage mechanized harvesting technology has become an urgent industry need (*Zhu et al., 2024; Xue et al., 2022; Zhai et al., 2018*).

The design of fruit and vegetable harvesting machinery must align closely with the physiological and structural characteristics of the target crops. Researchers worldwide have conducted extensive studies across a variety of horticultural products (*Barth et al., 2016; Tasneem et al., 2024; Hui et al., 2022; Lehnert et al., 2022*). For example, *Hohimer et al. (2019)* in the United States developed a pneumatic soft end-effector that achieved a 67% success rate in apple harvesting. In China, research on mechanized fruit and vegetable harvesting has continued to progress (*Tong et al., 2023; Yang et al., 2025; Wei et al., 2021; Jin et al., 2014; Zhang et al., 2023; Yu et al., 2023; Yin et al., 2017; Xu et al., 2018*).

Lu et al. (2020) at Nanjing Agricultural University designed a flexible gripper tailored to the delicate physical properties of brown mushrooms, enabling low-damage harvesting through a twisting motion. Similarly, Guo et al. (2023) at Shihezi University developed an underactuated harvesting mechanism for Korla fragrant pears, effectively improving adaptability to variable fruit size and orientation. However, research on endeffectors specifically adapted to the irregular shape and high bruise susceptibility of sweet peppers remains limited, and harvesting in greenhouse environments still relies predominantly on manual labor.

Considering the growth characteristics of sweet peppers and the current state of harvesting technology, this paper proposes a linkage-based underactuated end-effector for sweet pepper harvesting. This mechanism uses a single motor to drive a spring differential system, controlling two fingers with three phalanges each to adaptively envelop the fruit in sequence, coupled with a pneumatic cutting module for peduncle separation. The focus is on the following research: (1) Analyzing the contact mechanics characteristics between the end-effector and sweet pepper, establishing a safe clamping force threshold; (2) Conducting kinematic simulation and parameter optimization of the enveloping process based on ADAMS software; (3) Building an experimental platform to verify harvesting performance, providing technical support for mechanized sweet pepper harvesting.

MATERIALS AND METHODS

Mechanism Composition of the Sweet Pepper Harvesting End-Effector

The sweet pepper harvesting end-effector primarily consists of a connection frame, an underactuated gripping mechanism, and a cutting mechanism (Fig. 1), with the underactuated gripping mechanism serving as the core component.

To accommodate the irregular shape of sweet peppers, this paper presents a two-finger, three-phalanx gripping mechanism actuated by a single motor, based on the underactuation principle and a spring-based differential structure. The mechanism organizes its six degrees of freedom into three groups that actuate sequentially, enabling phased rotation of the phalanges to achieve adaptive enveloping. Key components of the gripping mechanism include underactuated fingers and their mounts, EVA cushioning material, flexible thin-film pressure sensors, a stepper motor, differential springs and push rods, a ball screw nut connection flange, a ball screw mechanism, and couplings. The cutting mechanism comprises pneumatic scissors, a linear mini-slide, an inclined cutting platform, and its connection frame.

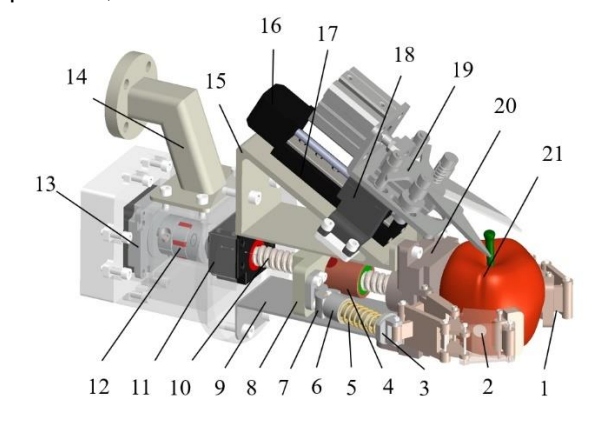


Fig. 1 - Structure diagram of end-effector

1. Underactuated finger; 2. Flexible thin-film pressure sensor; 3. Differential upper push rod; 4. Lead screw nut; 5. Differential spring; 6. Differential lower push-rod; 7. Lower push-rod fixed base; 8. Ball screw nut connecting flange; 9. Lower baffle; 10. Ball screw; 11. Ball screw limit block; 12. Coupling; 13. Stepper motor; 14. Connection frame; 15. Inclined cutting platform; 16. Linear slide motor; 17. Linear mini-slide; 18. Pneumatic scissor mounting bracket; 19. Pneumatic scissors; 20. Underactuated finger base; 21. Sweet pepper model.

Working Principle

As an end-effector of harvesting machinery, the manipulator works in coordination with the robotic arm to perform fruit picking. The harvesting process primarily consists of two stages: fruit gripping and peduncle cutting.

At the start of the operation, the manipulator's fingers are fully open to ensure the sweet pepper is within the operable workspace. The robotic arm adjusts the equatorial plane of the sweet pepper to be parallel with the horizontal plane of the manipulator and positions it at the center of the grasping space. Once the finger base contacts the equatorial contour of the pepper, the robotic arm halts. The stepper motor then activates, driving the ball screw to push the differential linkage mechanism, thereby actuating the two fingers to envelop the fruit progressively.

During the gripping phase, the proximal phalanx first contacts the fruit surface and is constrained by the contact reaction force, ceasing its motion. Subsequently, the middle phalanx rotates until it contacts the fruit, followed by the distal phalanx, which continues to complete the envelopment, forming a sequential adaptive envelopment. When the flexible thin-film sensors mounted on the inner side of the fingers detect that the normal pressure at all measured points has reached the predefined safety threshold, the motor stops.

After gripping is completed, the linear mini-slide carries the pneumatic scissors downward along the inclined guide platform. Once the peduncle enters the shearing zone, the cylinder actuates the scissors to swiftly sever it. The robotic arm then transports the harvested fruit to the collection area, where the gripping mechanism releases and resets, completing the single-fruit harvesting cycle.

End-Effector Finger Size Design and Workspace

This study focuses on commonly available red sweet pepper varieties. 50 mature fruits were selected for size measurement. Experimental results show the maximum contour diameter of the fruit is 102.54 mm, and the minimum contour diameter is 70.37 mm. To achieve effective enveloping and gripping of the fruit by the underactuated fingers, it is necessary to ensure the finger workspace covers the sweet pepper contour size range and establish a model (Fig.2), l_I , l_2 , l_3 represent the lengths of the proximal, middle, and distal phalanges, respectively. Push rods l_5 , l_6 and the spring form the spring differential mechanism. The two push rods are connected by a sliding pair, and the spring compression varies with the size of the gripped sweet pepper. θ_0 is the angle of the proximal phalanx relative to the horizontal direction. When θ_0 is 50°, the gripping diameter D_{min} is 70 mm. When θ_0 is 65°, the effective gripping range of the finger is maximized, with a gripping diameter of D_{max} being 103 mm.

To determine the optimal combination of phalanx lengths, the lengths of the three phalanges are defined as design variables, as shown in equation (1):

$$X = [l_1, l_2, l_3]^T \tag{1}$$

where: l_1 is the proximal phalanx length, m; l_2 is the middle phalanx length, m; l_3 is the distal phalanx length, m. The objective function f(x) is set as:

$$f(X) = w_1 \cdot |D(50^\circ) - 70| + w_2 \cdot |D(65^\circ) - 103| + w_3 \cdot P_c(X)$$
 (2)

where: D (50°) and D (65°) represent the gripping diameter of the end-effector when the proximal phalanx angle is 50° and 65° respectively, mm; $P_c(X)$ represents the collision penalty term; w_I , w_2 , w_3 are weight coefficients. Based on the workspace matching principle, parametric modeling and motion trajectory analysis were conducted using CAD, indicating that the phalanx lengths need to satisfy the following constraints:

$$\begin{cases} 30 \le l_1 \le 50 \\ 20 \le l_2 \le 40 \\ 10 \le l_3 \le 25 \end{cases} \tag{3}$$

$$\begin{cases} (\min)d_{\operatorname{tip}(\theta_0)} \ge 9 \\ 50^{\circ} \le \theta_0 \le 65^{\circ} \end{cases} \tag{4}$$

where: $(min)d_{tip(\theta\theta)}$ represents the minimum distance between the fingertips of the two distal phalanges at different θ_0 . Based on CAD simulation data, where θ_I denotes the rotation angle of the middle phalanx relative to the proximal phalanx, and θ_2 denotes the rotation angle of the distal phalanx relative to the middle phalanx. The rotation angle function of the middle phalanx relative to the proximal phalanx $\alpha(\theta_1)$ and the rotation angle function of the distal phalanx relative to the middle phalanx $\beta(\theta_2)$, obtained via least squares fitting, are expressed as:

$$\alpha(\theta_1) = -0.6364\theta_0 + 177.6364 \tag{5}$$

$$\beta(\theta_2) = -0.8545\theta_0 + 186.6818 \tag{6}$$

The phalanx coordinates of the end-effector were calculated based on the above rotation angle functions, and the MATLAB genetic algorithm toolbox was used to solve equation (2). The optimal phalanx length combination obtained was: l_l is 40.57 mm, l_2 is 33.77 mm, l_3 is 17.44 mm.

To verify if this result meets the design requirements, numerical validation was performed on the optimal solution: when θ_0 was 50° , the gripping diameter was 70.12 mm (target value 70 mm), with an error of 0.12 mm; when θ_0 was 65° , the gripping diameter was 102.89 mm (target value 103 mm), with an error of 0.11 mm; the minimum fingertip distance $(min)d_{tip(\theta\theta)}$ was 9.23 mm (requirement \geq 9 mm). These results demonstrate that the optimized phalanx dimensions enable the end-effector to accurately cover the target fruit diameter range of 70–103 mm, while ensuring no collision occurs between the distal phalanges during motion, thereby meeting the operational requirements for stable harvesting.

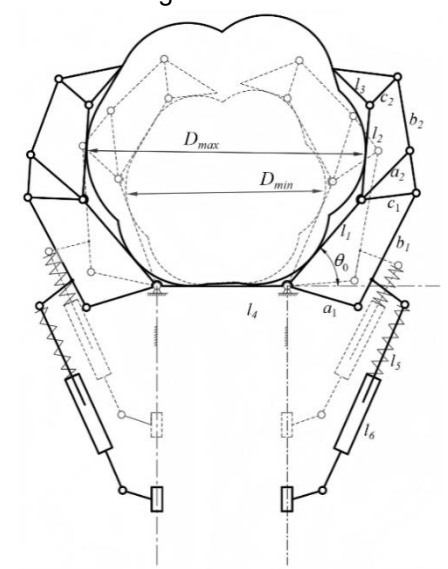


Fig. 2 - Size of finger joints and work space

Sweet Pepper Force Analysis

Due to the irregular surface shape of the sweet pepper, there are 6 contact points between the underactuated fingers and the fruit's surface. The force at each contact point i includes normal force N_i , horizontal friction force f_i , and vertical friction force f_i . The specific force analysis is shown in Fig.3.

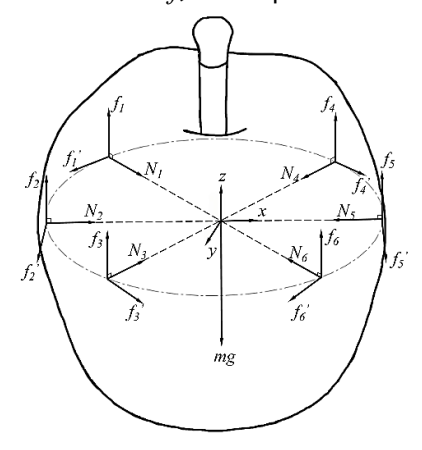


Fig. 3 - Mathematical model and stress analysis of sweet pepper

During gripping, the vertical friction force f_i needs to overcome the gravity of the sweet pepper to prevent fruit dropping, as expressed by the mechanical condition in equation (7). Based on the workspace analysis of the underactuated fingers in Fig. 3, the enveloping areas and force points on both sides of the sweet pepper are roughly symmetrical, and the horizontal forces can be considered symmetrically distributed. Let the minimum normal force be N_{min} . It should satisfy equation (8) to ensure no slipping occurs when gripping the fruit with maximum mass:

$$\sum_{i=1}^{6} f_i \ge mg \tag{7}$$

$$N_{\min} \ge \frac{m_{\max} g}{6\mu} \tag{8}$$

$$N_{\min} \ge \frac{m_{\max} g}{6\mu} \tag{8}$$

where: m_{max} is the maximum mass of the sweet pepper fruit, kg; g is the gravitational acceleration, taken as 9.8 m/s²; μ is the coefficient of friction between the sweet pepper surface and the cushioning material (EVA).

The measured maximum mass of sweet peppers was approximately 280 g. To determine the minimum normal force N_{min} , and considering individual variations, a maximum fruit mass m_{max} of 300 g was adopted (margin coefficient 1.07, gripping margin 7.14%). The coefficient of friction between the inner cushioning material (EVA) and the sweet pepper skin is 0.68. Substituting into equation (8) yields the minimum normal force N_{min} as 0.72 N. To ensure the normal force during end-effector gripping does not damage the sweet pepper's biological tissue, the maximum normal force N_{max} for non-destructive harvesting was determined by conducting sweet pepper compression experiments: 10 sweet peppers of different shapes were selected and divided into 2 groups. A circular indenter with a contact area of 40 mm² was used for loading at rates of 1.5 and 3 mm/s, respectively. The load-displacement curves obtained are shown in Fig. 4.

Experimental results show that under different loading speeds, the yield point of the sweet pepper skin appears between displacements of 12.5–20 mm, and skin rupture occurs successively between displacements of 35–50 mm. When the displacement is less than 12.5 mm, the load-displacement curve can be fitted as a linear relationship. Therefore, the displacement of 12.5 mm is considered the limit point of elastic deformation for the sweet pepper skin. To avoid biological damage caused by excessive displacement, the maximum allowable displacement is set to 12.5 mm, corresponding to a maximum normal force N_{max} of 33.56 N. In summary, the safe threshold for gripping normal force is 0.72–33.56 N.

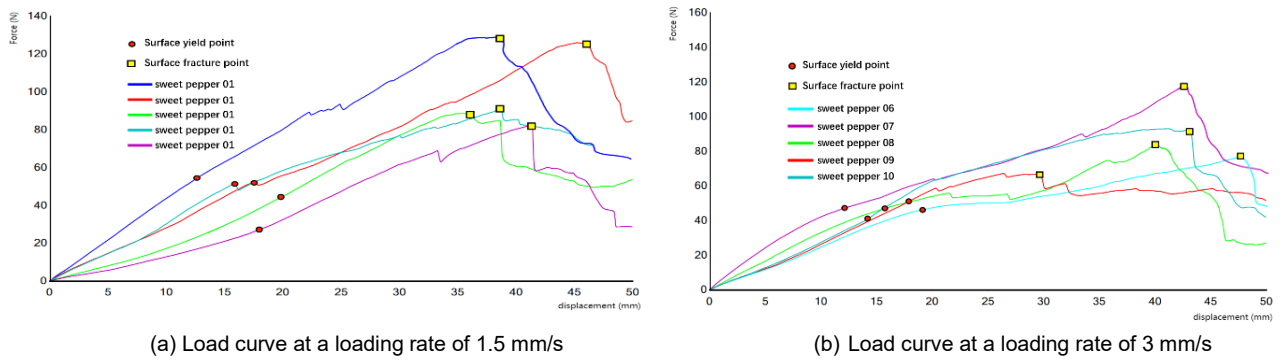


Fig. 4 - Displacement curves for different loading speed loads

Gripping Mechanism Force Analysis

The gripping stability of fruit and vegetable harvesting end-effectors directly affects the success rate. This paper establishes a complete static model based on the motion transmission chain for the ball screw-driven underactuated gripping mechanism (Fig. 5), focusing on analyzing the influence mechanism of the differential push rod inclination angle on force transmission efficiency, providing a theoretical basis for structural optimization.

In the first stage of the gripping process, the fingers have not contacted the fruit. The differential upper push rod slides relative to the lower push rod, compressing the spring.

The force balance equations at this stage are:

$$F_{\text{push}} = \frac{F}{\cos \theta} \tag{9}$$

$$F_{\text{push}} = F_{\text{spring}} = k \left(\delta + \delta_0 \right) \tag{10}$$

where: F is the slider thrust, N; θ is the angle between the differential lower push rod and the vertical direction, (°); F_{push} is the thrust force along the push rod direction, N; F_{spring} is the spring force, N; δ is the initial spring compression, mm; δ_0 is the additional compression during gripping, mm.

In the second stage of the gripping process, the fingers contact and gradually complete enveloping, reaching static equilibrium. At this point, the spring force acts as an internal force and does not affect the overall external force.

The thrust force along the push-rod direction is decomposed into components:

$$F_{\text{tangential}} = F_{\text{push}} \sin \varphi \tag{11}$$

$$F_{\rm radial} = F_{\rm push} \cos \varphi \tag{12}$$

where: $F_{tangential}$ is the tangential component of the thrust along the rod, N; F_{radial} is the radial component of the thrust along the rod, N; φ is the angle between the differential upper push rod and the finger link, (°).

Assuming the gripping mechanism is ideal (i.e., neglecting friction and inertial forces), the forces on the finger mechanism are simplified to point O. The moment equilibrium equation is established as shown in Eq. (13):

$$\sum M_O = M_{\text{pressure}} + M_{\text{push}} = 0 \tag{13}$$

where: $M_{pressure}$ is the resultant moment of the contact forces relative to point O, $N \cdot m$; M_{push} is the resultant moment of the thrust along the rod relative to point O, $N \cdot m$. Substituting the forces:

$$F_1 \cdot d_1 + F_2 \cdot d_{2'} + F_3 \cdot d_{3'} = F_{\text{tangential}} \cdot d_0 \tag{14}$$

$$F_2 = F_1 \cdot \cos \theta_1 \tag{15}$$

$$F_3 = F_2 \cdot \cos \theta_2 \tag{16}$$

$$d_0 = L \cdot \cos(\varphi - \theta) \tag{17}$$

From equations (9), (11), (14), (15), (16), (17), it can be derived the equation for the normal force F_I on the proximal phalanx as shown in Eq. (18):

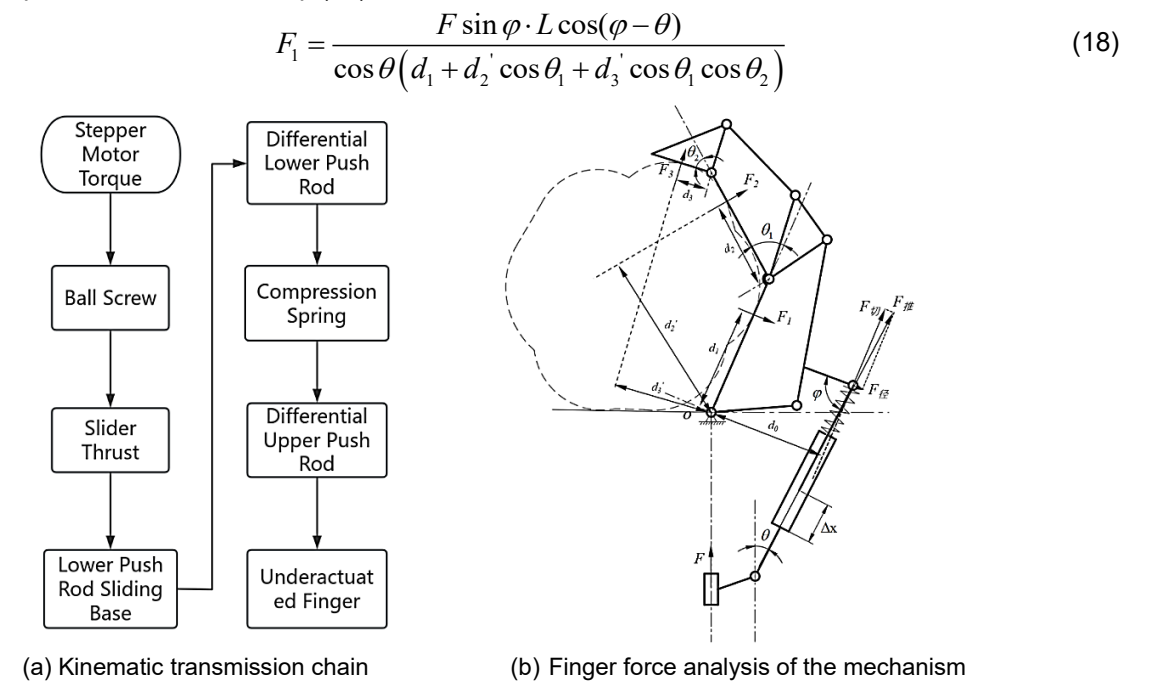


Fig. 5 - Kinematic transmission chain and finger force analysis of the mechanism

where: F_l is the normal force on the proximal phalanx, N; F is the slider thrust converted by the ball screw, N; L is the total length of the differential push rod in the current enveloping state, mm; d_l is the vertical distance between the proximal phalanx contact point and point O, mm; d_l is the vertical distance between the middle phalanx contact point and point O, mm; d_l is the rotation angle of the middle phalanx relative to the proximal phalanx, (°); θ_l is the rotation angle of the distal phalanx relative to the middle phalanx, (°).

Analysis of equation (18) shows that under stable gripping posture conditions, the proximal phalanx contact force F_l is influenced by multiple geometric and motion parameters, including the total push rod length L, the equivalent moment arms d_l , d_2 , d_3 of each phalanx, the phalanx rotation angles θ_l , θ_2 , the push rod angle φ , and the angle θ between the differential lower push rod and the vertical direction, among other angle and rod length parameters. Among these, L, d_l , d_2 , d_3 , θ_l , θ_2 vary with the fruit shape and enveloping state, and φ also changes dynamically with θ . To clarify the influence mechanism of key parameters, this study considers a fixed gripping posture, in which L, d_l , d_2 , d_3 , θ_l , θ_2 are determined and treated as constants. Thus, the angle θ between the lower differential push rod and the vertical direction is selected as the controllable variable for parameter optimization.

According to the finger spatial configuration in Fig. 3, when gripping smaller fruits (e.g., fruit diameter 70 mm), θ reaches its maximum value. Taking this as a typical working condition, set L is 78 mm, d_I is 22.8 mm, d_Z is 42 mm, d_Z is 39.5 mm, θ_I is 58.17°, θ_I is 33°. Substitute these into the static model for calculation. The results are shown in Table 1, where F represents the slider thrust; since the lead screw is not yet selected, it is represented by a symbol.

Table 1

Influence of different 8 values on proximal phalanx contact force F1		
θ/ (°)	φ /(°)	F1/(N)
0	120	0.54F
5	115	0.39F
10	110	0.21F
15	105	0

Calculation results show that as θ increases, the axial force of the push rod increases non-linearly, leading to a significant attenuation in the effective contact force, which drops to zero at 15°, indicating a kinematic dead center. Therefore, to avoid mechanism failure and ensure gripping reliability, θ must be strictly kept below 15°. Further considering uncertainties and safety margins in actual working conditions, the reasonable range for θ is finally determined as 5°≤ θ ≤10°.

Substituting the maximum allowable normal force N_{max} =33.56 N obtained from the previous sweet pepper compression experiment and the above range of θ into equation (18), the required range of slider thrust F is calculated inversely as $86.49\text{N} \le F \le 162.13\text{N}$. Based on the range of θ and the mechanism motion requirements, the effective stroke of the lead screw is determined to be 130 mm. Considering the nut size and installation space, the lead screw length is finally selected as 180 mm. The standard ball screw model SFU1205 is selected. The transmission efficiency between the motor and the lead screw is taken as 0.9. The required motor torque is calculated as 0.29 N·m according to equation (19). A NEMA23 stepper motor (model 23HS5628) is actually selected, with a rated torque of 1.26 N·m, meeting the torque requirement with sufficient margin.

$$T = \frac{F_{\text{axial}}I}{2\pi\eta} \tag{19}$$

where: T is the motor torque, N·m; F_{axial} is the axial load on the lead screw, equal to 2F, N; I is the lead of the lead screw, mm; η is the transmission efficiency between the motor and the lead screw.

Simulation Model and Parameter Settings

Based on the determined underactuated finger length mechanism parameters, differential push rod vertical inclination angle, and other mechanism parameters from the previous sections, combined with sweet pepper biomechanical characteristics, a kinematic model was built in ADAMS as shown in Figure 6.

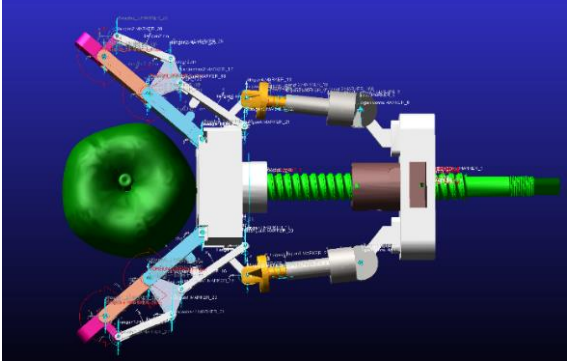


Fig. 6 - Constraint settings of the simulation model

First, the end-effector model from SolidWorks was exported in .x_t format and imported into the simulation software. Key moving parts (fingers, push rods, lead screw, etc.) were retained, while non-critical structures (bolts, decorative parts, etc.) were simplified. A flexible geometric body was created based on the measured sweet pepper dimensions as the gripping model and imported together with the end-effector model. Revolute joints were set at the finger phalange hinges, sliding pairs were set between push rods, the stiffness of the differential spring set was set to 5 N/mm, the spring precompression was set to 15 mm. A rotational velocity drive was applied to the lead screw, defined by the function step (time, 0, 0, 5, 600d).

Here, "600d" denotes the final steady-state rotational speed of the lead screw, indicating that it rotates at an angular velocity of 600 °/s.

The contact parameters between the cushioning material on the underactuated finger surface and the sweet pepper skin are crucial factors affecting the simulation results and require calculation and verification. Since the contact between the sweet pepper and the end-effector finger can be approximated as contact between a sphere and a plane, the Hertz contact model for sphere-plane contact is used. The Hertz theory gives the relationship between contact force F and deformation δ in equation (20):

$$F = \frac{4}{3}E^*\sqrt{R}\delta^{\frac{3}{2}} \tag{20}$$

where:

F is the contact force between the finger and the sweet pepper surface, N; E^* is the equivalent elastic modulus, MPa; R is the radius of curvature of the sweet pepper at the contact point, mm; δ is the deformation of the sweet pepper skin, mm.

Although the sweet pepper surface is irregular, the contact point can be approximated as spherical. Based on geometric relations, the radius of curvature of its cross-sectional contour can be taken as 40 mm. The reasonable deformation of the sweet pepper skin can be determined from the previous compression experiment as 12.5 mm. The measured elastic modulus of the sweet pepper is 1.2 MPa, Poisson's ratio is 0.35; the elastic modulus of the EVA material is taken as 12 MPa, Poisson's ratio as 0.4.

Substituting into equation (21) yields E^* is 1.235MPa.

$$\frac{1}{E^*} = \frac{1 - \nu_1^2}{E_1} + \frac{1 - \nu_2^2}{E_2} \tag{21}$$

where: E_I and v_I are the elastic modulus and Poisson's ratio of the sweet pepper, E_2 and v_2 are the elastic modulus and Poisson's ratio of the EVA material.

The contact stiffness calculation formula can be derived from equation (20) as (22):

$$K = \frac{dF}{d\delta} = 2E^* \sqrt{R} \sqrt{\delta}$$
 (22)

Substituting the known quantities above yields a contact stiffness K of 55.328 N/mm. Considering both safety factors and simulation margins, K is set as 60 N/mm in this study. The grasping posture of the simulation model is shown in Fig. 7.

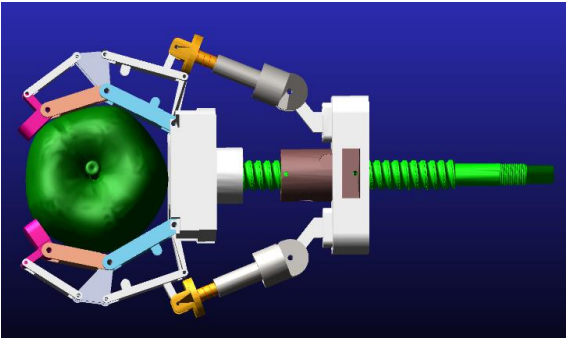


Fig. 7 - Grasping posture of the simulation model

Kinematics and Contact Characteristics Verification

The phalanx rotation angle time-history curve obtained from the simulation results (Fig. 8) quantitatively verifies the mechanism's motion characteristics: First, the proximal phalanx starts moving. After the proximal phalanx completes envelopment, the middle phalanx begins to rotate. At approximately 2.5 s, the middle phalanx contacts the sweet pepper surface, forming a closed constraint. At this point, the revolute joint between the middle and distal phalanges becomes the working DOF, and the distal phalanx rotates. The overall enveloping process follows the proximal-middle-distal driving sequence. Meanwhile, quantitative analysis based on the single-side phalanx contact force time-history curve (Fig. 9) shows the highest peak is the proximal phalanx contact force at about 4.8 s, with a value of about 15.89 N, which is less than the maximum normal force threshold of 33.56 N, meeting the non-damaging condition; the lowest peak is the distal phalanx contact force at about 4.8 s, with a value of about 5.75 N, which is greater than the minimum normal force threshold of 0.72 N, meeting the anti-slip condition.

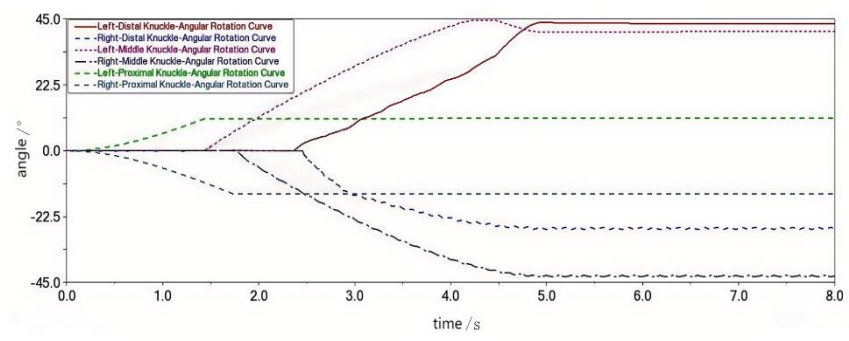


Fig. 8 - Time-history curve of joint rotation angle

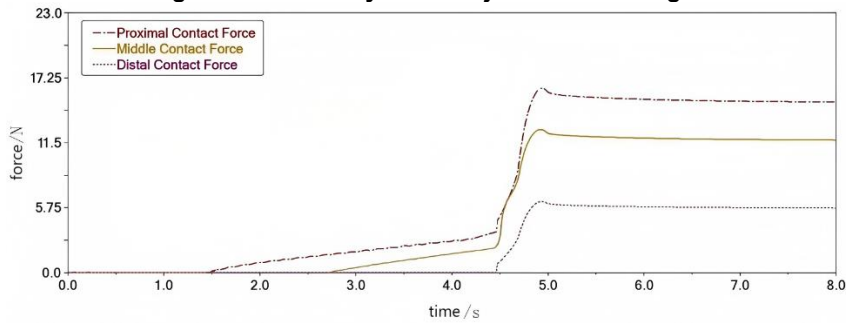


Fig. 9 - Time-history curve of contact force on a single-side joint

Design of the Electric Control System

To achieve automated operation for the linkage-based underactuated sweet pepper harvesting manipulator, this paper designs an electric control system using an Arduino MEGA2560 as the main controller. By coordinating the gripping stepper motor, the cutting stepper motor, and the pneumatic solenoid valve, the system strictly adheres to the working principle of "adaptive enveloping gripping first, followed by precise cutting." It utilizes real-time feedback from flexible thin-film pressure sensors to monitor the gripping force, ensuring it remains within the threshold range between non-damaging and anti-slip limits, thereby achieving accurate positioning and cutting of the fruit stem. The core workflow of this control system strictly follows the working principle of the manipulator, as shown in Fig.10.

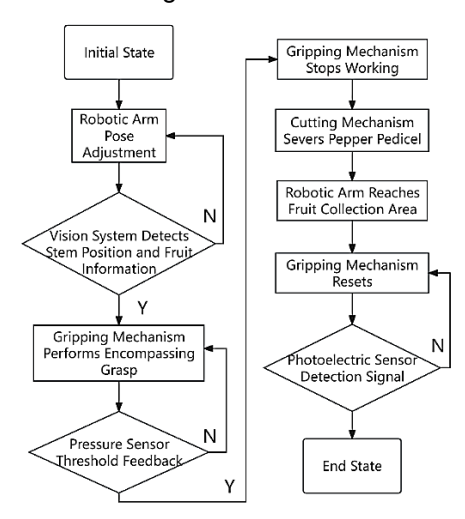


Fig. 10 - Flowchart of the end-effector control program

The electric control system adopts a modular architecture, comprising the main control, sensor, drive, actuator, and power supply modules. The main control module, centered around the Arduino MEGA2560 microcontroller, is responsible for signal processing and control output. The sensor module includes six flexible thin-film pressure sensors and a limit switch, used for detecting the gripping normal force and the homing position of the linear slide, respectively. The drive module consists of stepper motor drivers and a relay module, controlling the gripping stepper motor, the cutting stepper motor, and the pneumatic solenoid valve accordingly. The actuator module includes a NEMA23 stepper motor for driving the ball screw to achieve finger enveloping, a 28BYJ-30 stepper motor for driving the linear mini-slide, and a low-voltage pneumatic solenoid valve for controlling the opening and closing of the pneumatic scissors.

RESULTS

Harvesting Experiment

Based on the previous design and simulation results, to determine the success rate, efficiency, and non-destructive harvesting effect of the sweet pepper harvesting device, a sweet pepper harvesting test platform was built. The platform consists of a mobile chassis and the harvesting end-effector, as shown in Fig.11.

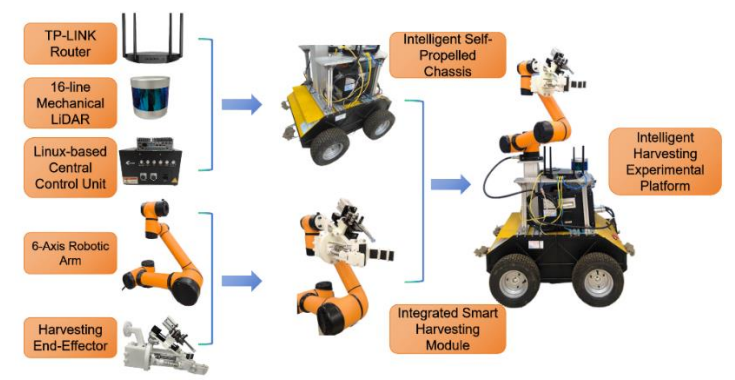


Fig. 11 - Sweet pepper harvesting test platform

The experimental platform consists of a mobile base equipped with a 6-DOF robotic arm (load capacity: 5 kg, repeatability: ±0.1 mm), to which the harvesting end-effector is fixed. During experiments, the manipulator was manually adjusted to align the central plane of the sweet pepper's maximum diameter contour with the gripping center of the end-effector, while maintaining a 40 mm distance between the fruit and the finger base. Harvesting failure was defined as the occurrence of any of the following: fruit dropping, incomplete peduncle severance, or the appearance of irreversible indentations on the fruit surface—defined as visible indentations that do not recover through the natural elasticity of the peel.

Based on prior design and simulation results, the stepper motor speed was found to significantly influence harvesting performance. Preliminary tests indicated that speeds exceeding 100 r/min considerably increased the risk of contact force overshoot, while stable enveloping gripping could be achieved within the 50–100 r/min range. To determine the optimal speed, a total of 120 ripe red sweet peppers with contour diameters ranging from 70 to 100 mm were selected as test samples. Comparative tests were conducted within the speed range of 80–100 r/min, during which single-fruit harvesting time, success rate, and damage rate were recorded (the test setup is shown in Fig.12, and results are presented in Table 2). The harvesting success rate was quantitatively determined using custom formula (23).

$$S = \frac{X}{X_{\text{total}}} \times 100\% \tag{23}$$

where: S represents the harvesting success rate of sweet pepper fruits at a single motor speed; X represents the number of successfully harvested individuals; X_{total} represents the total number of individuals harvested at the set speed.

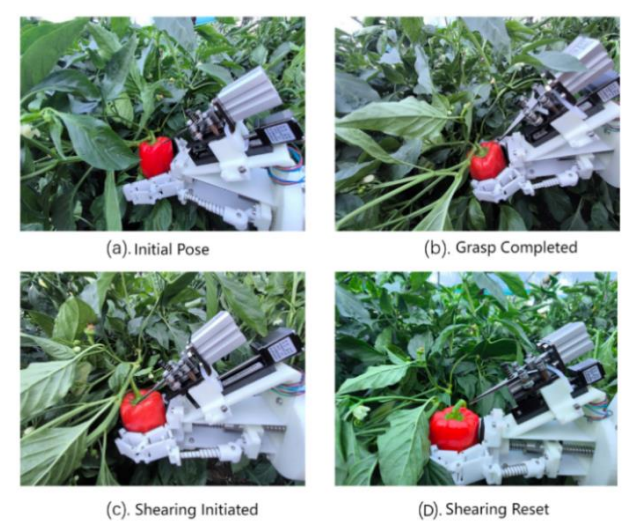


Fig. 12 - Experiment of sweet pepper picking

Table 2

Harvesting indicators at	different stepper motor speeds
--------------------------	--------------------------------

Stepper motor speed (r/min)	Single fruit harvesting time (s)	Harvesting success rate (%)	Damage rate (%)
80	24.21	82.76	0
85	22.92	84.68	0
90	21.70	89.34	0
95	20.57	84.34	0
100	19.54	81.26	0

Discussion and Results

Analysis of Table 2 shows that the single fruit harvesting time decreases with increasing stepper motor speed. The harvesting time is lowest at 100 r/min, at 19.54 s. However, starting from 95 r/min, the harvesting success rate relatively decreases. The highest harvesting success rate was achieved at a motor speed of 90 r/min, reaching 89.34%. Experiments also confirmed that the sweet pepper skin damage rate is not affected by changes in motor speed. At stepper motor speeds of 90 and 100 r/min, the single fruit harvesting time differs by 2.16 s, but the success rate at 90 r/min is 9.94% higher than at 100 r/min. Therefore, since the increase in harvesting speed is not substantial, to maintain a higher success rate, 90 r/min is considered the optimal motor speed for sweet pepper harvesting with this mechanism. At this speed, the single fruit harvesting time is 21.70 s, and the success rate is 89.34%. Analysis of the harvesting failure cases revealed that the main contributing factors were: excessive bending of the peduncle in some sweet pepper individuals, leading to too small a gap between the peduncle and the fruit surface, causing damage to the fruit because the scissors lacked sufficient workspace. Also, due to the complex growth posture of sweet peppers, situations where two fruits grow on the same plant node can occur. This situation affects the finger's ability to grasp and envelop the target fruit.

CONCLUSIONS

- (1) Based on the underactuated principle and a spring-based differential mechanism, a two-finger, three-phalanx gripper driven by a single motor was designed, integrated with pneumatic scissors to form the end-effector. Through spring differentials and push-rod transmission, the mechanism achieves sequential adaptive rotation of the proximal-middle-distal phalanges, effectively enveloping the irregular shape of sweet peppers while maintaining six-point contact. Workspace analysis indicated a gripping diameter range of 70–103 mm, covering typical sweet pepper dimensions, and a static model confirmed its stable gripping capability.
- (2) Biomechanical compression tests on sweet peppers determined the maximum non-destructive gripping force threshold to be 33.56 N and the minimum anti-slip threshold to be 0.72 N. Static analysis of the differential push-rod mechanism revealed that the push rod inclination angle θ significantly influences force transmission efficiency, with an optimized range of 5°–10° to avoid dead centers and ensure sufficient contact force. Accordingly, a ball screw (SFU1205) and a stepper motor (23HS5628) were selected, providing an output torque of 1.26 N·m, which meets the theoretical slider thrust requirement of 86.49–162.13 N. ADAMS dynamic simulation further verified that the mechanism's motion sequence was correct and that the peak contact force of 15.89 N remained within the safe threshold, satisfying non-damaging and anti-slip requirements.
- (3) Performance tests conducted on a built experimental platform showed that the stepper motor speed significantly affected the picking success rate and efficiency. The highest success rate (89.34%) was achieved at 90 r/min, with a single fruit picking time of 21.70 s. Deviation from this speed resulted in a decreased success rate. The damage rate was 0% across all tested speeds, verifying the non-damaging nature of the mechanism. Excessive peduncle curvature and dense fruit growth were identified as the main non-mechanical factors leading to failures. Comprehensive performance evaluation indicates that 90 r/min is the optimal motor speed for sweet pepper harvesting with this mechanism.

ACKNOWLEDGEMENT

This research was funded by the National Natural Science Foundation of China (No:31971801), the Natural Science Foundation of Shandong Province of China (No: ZR2020ME252, ZR2020ME250) and Qingdao Science and Technology Benefit-the-People Demonstration Project(25-1-5-xdny-33-nsh).

REFERENCES

- [1] Barth, R., Hemming, J., &Van Henten E.J. (2016). Design of an eye-in-hand sensing and servo control framework for harvesting robotics in dense vegetation. *Biosystems Engineering*, 146: 71-84.
- [2] Chen M.J., & He T. (2025). Global Vegetable Industry Development Status. *China Fruits and Vegetables*, 45(05): 1-8.
- [3] Guo, H.S., Ma, R., Zhang, Y.X., & Li, Z.Y. (2023). Design and simulation analysis of a Y-shaped underactuated manipulator for Korla fragrant pear harvesting. *Journal of Agricultural Mechanization Research*, 45(01), 110–117.
- [4] Hohimer, C.J., Wang, H., Bhusal, S., Miller, J., Mo, C., & Karkee, M. (2019). Design and Field Evaluation of a Robotic Apple Harvesting System with a 3D-Printed Soft-Robotic End-Effector. *Trans. ASABE*, 62(2), 405–414.
- [5] Hui, Y.T., Liao, Y.Y., Wang, D.C., Li, X.X., Lu, Z.H., You, Y., & Jia, H.C. (2023). Design and Experiment of an End-Effector for Harvesting Sweet Pepper in Compliant Obstacle Environment. *INMATEH-Agric. Eng*, 71(3), pp.271-281. DOI: https://doi.org/10.35633/inmateh-71-23
- [6] Jin, B., & Lin, L.X. (2014). Design and force control of an underactuated gripper for fruit and vegetable picking. *Journal of Mechanical Engineering*, 50(19), 1–8.
- [7] Lehnert, C., McCool, C., Sa, I., & Perez, T. (2020). Performance Improvements of a Sweet Pepper Harvesting Robot in Protected Cropping Environments. *J. Field Robot*, 37(7), 1197–1223.
- [8] Lu, W., Wang, P., Wang, L., & Deng, Y.M. (2020). Design and experiment of a flexible gripper for non-destructive picking of brown mushroom. *Transactions of the Chinese Society for Agricultural Machinery*, 51(11), 28–36.
- [9] Tasneem, Z., & Oka, K. (2024). Design and performance analysis of soft pneumatic manipulator-based linear cutter and stem holder for sweet pepper harvesting. *Journal of Field Robotics*, 41(4): 1204-1225.
- [10] Tong, Y., Zhang, H., Zhong, J.P., Wu, F., & Liu, S.H. (2023). Design of a flexible end-effector for tomato picking. *Journal of Heilongjiang University of Technology (Comprehensive Edition*), 23(10), 141–149.
- [11] Wei, B., He, J.Y., Shi, Y., Jiang, G.L., Zhang, X.Y., & Ma, Y. (2021). Design and experiment of an underactuated end-effector for citrus harvesting. *Transactions of the Chinese Society for Agricultural Machinery*, 52(10), 120–128.
- [12] Wang, Y.M., Hao, D.C., Si, Y., Wu, Q.H., Zhang, J., & Liu, S.H. (2023). Soilless cultivation techniques for fruit-type sweet pepper in South China during long seasons. *Agricultural Science and Technology Communication*, (10), 204–206.
- [13] Xu, L.M., Liu, X.D., Zhang, K.L., Xing, J.J., Yuan, Q.C., Chen, J.W., Duan, Z.Z., Ma, S., & Yu, C.C. (2018). Design and experiment of an end-effector for navel orange harvesting robot. *Transactions of the Chinese Society of Agricultural Engineering*, 34(12), 53–61.
- [14] Xue, R.X. (2022). Recognition and picking system for sweet pepper harvesting robot in greenhouse. *Journal of Longdong University*, 33(02), 57–62.
- [15] Yang, X.Y., Yang, Q.Z., Liu, L., Zhong, X., & Qu, G.Y. (2025). Design and experiment of an end-effector for facility tomato harvesting robot. *Journal of Agricultural Mechanization Research*, 47(11), 126–134.
- [16] Yin, J.J., Chen, Y.H., He, K., & Liu, J.Z. (2017). Design and experiment of a grasping-rotating underactuated two-finger device for grape harvesting. *Transactions of the Chinese Society for Agricultural Machinery*, 48(11), 12–20.
- [17] Yu, L., Yu, G.H., Wu, H.Y., Sun, F.X., & Qian, M.B. (2023). Design and experiment of an underactuated articulated end-effector for citrus harvesting. *Transactions of the Chinese Society of Agricultural Engineering*, 39(17), 29–38.
- [18] Zhai, Y.H., Deng, Z.H., & Zhang, J.X. (2018). Research progress on end-effectors for greenhouse harvesting robots. *Agricultural Engineering Technology*, 38(22), 22–28.
- [19] Zhang, Y.Y., Tian, J.Q., Wang, W.X., Zhou, J.L., Wang, J.P., & Hu, H.R. (2023). Design and experiment of an end-effector for pitaya harvesting robot. *Journal of Forestry Engineering*, 8(04), 144–150.
- [20] Zhu, Z.W., Liu, K.G., Song, Y.P., & Li, L.M. (2024). Effects of planting density and pruning methods on plant growth and fruit quality of sweet pepper. Shanghai Vegetables, (03), 56–59.